PHYSICAL REVIEW B **106**, 224107 (2022)

Origin of negative electrocaloric effect in *Pnma*-type antiferroelectric perovskites

Ningbo Fan,[1] Jorge Íñiguez,[2,3] L. Bellaiche,[4] and Bin Xu[1,*]

[1]*Institute of Theoretical and Applied Physics, Jiangsu Key Laboratory of Thin Films, School of Physical Science and Technology, Soochow University, Suzhou 215006, China*

[2]*Materials Research and Technology Department, Luxembourg Institute of Science and Technology (LIST), Avenue des Hauts-Fourneaux 5, L-4362 Esch/Alzette, Luxembourg*

[3]*Department of Physics and Materials Science, University of Luxembourg, Rue du Brill 41, L-4422 Belvaux, Luxembourg*

[4]*Physics Department and Institute for Nanoscience and Engineering, University of Arkansas, Fayetteville, Arkansas 72701, USA*

(Received 22 March 2022; revised 8 December 2022; accepted 9 December 2022; published 19 December 2022)

Electrocaloric materials of solid state hold great promise for next-generation high-efficiency cooling technology. Besides the normal electrocaloric effect (ECE) in ferroelectrics or relaxors, anomalous ECE with decreasing temperature upon application of an electric field is known to occur in antiferroelectrics (AFEs), and previous understanding refers to the field-induced canting of electric dipoles if there is no phase transition. Here we use a first-principles-based method to study the ECE in Nd-substituted $\mathrm{BiFeO_3}$ (BNFO) perovskite solid solutions, which has a *Pnma*-type AFE ground state. We demonstrate another scenario to achieve and explain anomalous ECE, emphasizing that explicit consideration of octahedral tiltings is indispensable for a correct understanding. This mechanism may be general for AFEs for which the antipolar mode is not the primary order parameter or for other commonly occurring *Pnma*-type perovskites, even without being AFEs. We also find that the negative ECE can reach a large magnitude in BNFO.

DOI: 10.1103/PhysRevB.106.224107

I. INTRODUCTION

Today's mainstream cooling technology for refrigeration and air conditioning has posed growing challenges as it consumes more than 20% of the generated electricity and causes serious greenhouse effect [1]. Electrocaloric effect (ECE) in solid-state materials can make temperature change via adiabatic application (or removal) of an electric field, providing an efficient approach for cooling or heating [2–4]. While ferroelectric (FE) or relaxor materials typically have a normal positive sign of ECE, i.e., the temperature increases by applying a voltage, antiferroelectrics (AFEs) are known to have an anomalous ECE that can yield an opposite sign [5–7]. These two types of ECE can be utilized in combination to improve the performance of cooling/heating devices.

Such a negative (or inverse) caloric effect is also known to occur in other occasions, e.g., magnetic Heusler alloys, transitions between FE phases of different polarization directions, and application of an electric field against the polarization of a FE phase without switching [8–10]; however, its origin in AFEs is less well understood. AFEs materials are characterized by antipolar atomic distortions that can be switched to a FE state under an electric field, and two mechanisms to explain their negative ECE with no AFE-FE transition have been proposed: (1) the dipole-canting model that dipolar entropy increases by misaligning the antiparallel dipoles upon application of the field [6] and (2) the perturbative theory based on the Maxwell relation that only temperature and electric field dependencies of polarization need to be considered [11]. Interestingly, all these mechanisms only take the electric degrees of freedom explicitly into account. In contrast, most of the known AFEs are neither the proper type (that is, the AFE phase is rarely driven by an AFE soft mode [12]) nor systems with the antipolar mode being the only significant order parameter. In fact, quite often, the AFE mode is secondary and coupled to other degrees of freedom, such as the octahedral tiltings in perovskites. For instance, $\mathrm{PbZrO_3}$ (PZO) has a strong instability of antiphase octahedral tilting [13], while in *Pnma*-type perovskite, being the most occurring ground-state space group among perovskites [14], such as in rare earth orthoferrites and $\mathrm{CsPbI_3}$, the antipolar distortion arises from the condensation of both the in-plane antiphase ($\omega_{R,(x,y)}$) and out-of-plane in-phase tiltings ($\omega_{M,z}$) via trilinear coupling [15]. Although these tilting modes are nonpolar, they couple strongly with the polar and antipolar modes so they can be influenced by the electric field as well and, as a consequence, contribute to the ECE.

To get a deeper understanding of the (negative) ECE in AFEs, analysis based on Landau models involving the most relevant degrees of freedom has been proved to be very useful [16–19], and it may thus be necessary that all the important order parameters are taken into consideration. Furthermore, some previous phenomenological models are often oversimplified, since only one dimension is assumed [5]. In reality, the direction of the applied field with respect to the crystallographic axis should have different effects regarding ECE.

In this paper, we take the AFE Nd-substituted $\mathrm{BiFeO_3}$ (BNFO) solid solution as an example and demonstrate that the octahedral tiltings can have a very important effect on

---

[*] binxu19@suda.edu.cn

the sign and magnitude of the ECE. We also construct a phenomenological model that allows us to rationalize the contributions of each degree of freedom. In particular, the dipoles alone are found to be insufficient to explain the negative ECE, while contributions from the in-phase and antiphase tilting modes are indispensible. Moreover, BNFO is predicted to yield rather large negative ECE close to the AFE-to-FE transition.

This paper is organized as follows. A description of the computational method is provided in Sec. II. Section III reports and discusses the structural change under electric field, decomposed contributions to the ECE, influence from the field direction, largest electrocaloric temperature, and verification of the dipole canting model. Finally, we summarize the study in Sec. IV.

II. METHODS

The solid solutions are simulated by a $12\times12\times12$ supercell (containing 8640 atoms) using Monte Carlo (MC) simulations, in which the Bi and Nd atoms are randomly distributed (see Supplemental Material (SM) Sec. S1 for details [20]). The total energy of this effective Hamiltonian can be expressed as a sum of two main terms:

$$E_{\text{tot}} = E_{\text{BFO}}(\{\boldsymbol{u}_i\}, \{\eta_H\}, \{\eta_I\}, \{\boldsymbol{\omega}_i\}, \{\boldsymbol{m}_i\}) + E_{\text{alloy}}(\{\boldsymbol{u}_i\}, \{\boldsymbol{\omega}_i\}, \{\boldsymbol{m}_i\}, \{\eta_{\text{loc}}\}), \quad (1)$$

where E_{BFO} is the effective Hamiltonian of pure BFO [21–24] and E_{alloy} characterizes the effect of substituting Bi by Nd ions.

This effective Hamiltonian contains four types of degrees of freedom: (1) the local modes $\{\boldsymbol{u}_i\}$ centered on the *A* sites (i.e., on Bi or Nd ions), which are proportional to the local electric dipole [25,26]; (2) the homogeneous $\{\eta_H\}$ and inhomogeneous $\{\eta_I\}$ strain tensors [25,26]; (3) the pseudovectors $\{\boldsymbol{\omega}_i\}$ that characterize the oxygen octahedral tiltings [27]; and (4) the magnetic moments $\{\boldsymbol{m}_i\}$ of the Fe ions. (In all cases, subscript i labels five-atom unit cells in our simulation supercells.) In this Hamiltonian, a local quantity $\eta_{\text{loc}}(i)$ centered on the Fe site i is also introduced as $\eta_{\text{loc}}(i) = \frac{\delta R_{\text{ionic}}}{8}\sum_j \sigma_j$, where σ_j (0 or 1) accounts for the presence of Bi or Nd ion at *A* site j and the sum over j runs over the eight nearest neighbors of Fe site i, and where δR_{ionic} represents the relative difference in ionic radius between Nd and Bi ions. $\eta_{\text{loc}}(i)$ is therefore different from zero if at least one of these eight *A* sites is occupied by Nd ions, while it vanishes for pure BFO. More details about this method can be found in Ref. [28] and references therein.

Under an applied electric field, an additional term $-\sum_i \boldsymbol{p}_i \cdot \boldsymbol{\mathcal{E}}$ is incorporated, where the local electric dipoles $\boldsymbol{p}_i$ are computed from the local modes $\{\boldsymbol{u}_i\}$ and effective charges Z_i^*. Moreover, we numerically find that the simulated $\mathcal{E}$ field is larger than the corresponding experimental field by an approximate factor of 23 (SM Sec. S1 [20]), which is considered for all reported field strengths. Note that this scale factor is obtained by fitting the simulated P-$\mathcal{E}$ loop of $Bi_{0.9}Nd_{0.1}FeO_3$ with available measured loops of $Bi_{0.94}Sm_{0.06}FeO_3$ and $Bi_{0.91}Sm_{0.09}FeO_3$ [29], under electric fields applied along the pseudocubic [111] direction at 300 K (Fig. S1, SM Sec. S1 [20]), which involves the *R*3*c* phase as the stable structure. A moderate difference in the scale factor may be expected for the *Pnma* phase that is studied in this paper. Also note that BNFO is multiferroic and, in principle, the magnetic moments can also respond to the applied electric field. Here it is not considered since we focus on the structural order parameters for a general AFE and numerically the magnetic contribution to α is found to the small (see Ref. [30]).

For the statistical distribution of electric dipole orientations and octahedral tilting angles at 300 K under zero and various fields (shown in Fig. 6), after reaching equilibrium, 20 snapshot structures in which all the dipoles and tiltings of the $12\times12\times12$ supercells are considered. The probability is computed by the ratio of the number of dipoles (or tiltings) with angles falling in the range between θ and $\theta+\Delta\theta$ (or between ϕ and $\phi+\Delta\phi$) and the total number, with $\Delta\theta$ (or $\Delta\phi$) being 3 degrees.

III. RESULTS AND DISCUSSION

A. Structural change under electric field

$BiFeO_3$ (BFO) stabilizes in a *R*3*c* ground state, but rare-earth doping with composition larger than 20–30% is sufficient to alter it to the *Pnma* structure (Fig. 1) [31]. Here, we use a first-principles-based effective Hamiltonian scheme [28] (see Methods section) to study the $Bi_{0.6}Nd_{0.4}FeO_3$ solid solution under electric field at finite temperatures. With this composition, BNFO is stabilized in the AFE *Pnma* phase at room temperature (RT) and can transform to a FE state under an electric field [28,31–34].

First, let us check how the order parameters are influenced by the electric field $\mathcal{E}$. Note that the initial *Pnma* structure has zero polarization, an in-plane anti-polar vector X along the [110] direction, and $a^-a^-c^+$ tilting in Glazer's notation (which corresponds to finite x and y components of the antiphase tilting vector, $\omega_{R,x} = \omega_{R,y}$, and finite z component of the in-phase tilting vector, $\omega_{M,z}$). Three representative field directions are investigated (Fig. 2), together with the zero-field data (dashed curves) for comparison (for other $\mathcal{E}$ magnitudes, see SM Sec. S2 [20]). With no applied field, the *Pnma* phase transforms to the paraelectric (PE) cubic phase at 1400 K (dashed lines in Fig. 2).

Under [001] field, we consider a representative case with $\mathcal{E} = 0.87$ MV cm^{-1}, with which the AFE state transforms to the FE *P*4*mm* phase at 880 K, characterized by a large polarization P_z along [001] and no octahedral tiltings. In the AFE state, one can see that the temperature dependence of $\omega_{M,z}$ does not differ much from the zero-field case, whereas P and $\omega_{R,(x,y)}$ ($\omega_{R,x} = \omega_{R,y}$) show apparent changes. The moderate field-induced change of X can be understood to a good approximation via the change in $\omega_{R,(x,y)}$ since $X_{(x,y)}$ should be proportional to the product $\omega_{R,(x,y)}\omega_{M,z}$ as a result of a trilinear coupling between $X_{(x,y)}$, $\omega_{R,(x,y)}$ and $\omega_{M,z}$ [35]. Finite P_z is induced by the field, whereas the field-induced suppression of $\omega_{R,(x,y)}$ is due to the competitive coupling with P_z.

Moreover, if the field is applied along $[1\bar{1}0]$ [Figs. 2(c) and 2(d)], P is induced along the same direction, i.e., a finite $P_x = -P_y$ first develops, and a transition to a FE *Cc* phase

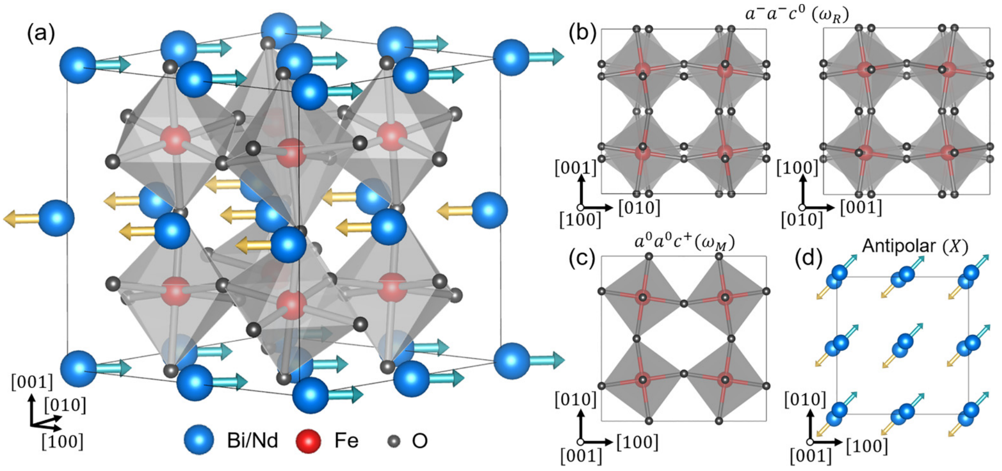

FIG. 1. Characteristics of the *Pnma* phase. (a) The *Pnma* structure of $\mathrm{Bi}_{1-x}\mathrm{Nd}_x\mathrm{FeO}_3$. (b) FeO_6 in-plane antiphase octahedral tilting ω_R ($a^-a^-c^0$ in Glazer's notation), viewed from [100] and [010] directions, respectively. (c) FeO_6 out-of-plane in-phase octahedral rotation ω_M ($a^0a^0c^+$ in Glazer's notation). (d) The antipolar vector X. The blue and yellow arrows represent local electrical dipoles in alternating planes.

occurs at 790 K, a structure characterized by a polarization in $\langle uuv\rangle$ direction ($u > v$) and $a^-a^-c^-$ octahedral tiltings ($a > c$). The third $\mathcal{E}$ direction is along [110], along which P develops, while $\omega_{M,z}$ is much suppressed and $\omega_{R,(x,y)}$ is more or less unchanged within the AFE-based state (by AFE-based state, we mean the AFE state with all its associated order parameters but on top of which polarization develops along the field direction). Such an AFE phase then also transforms into a *Cc* phase at 780 K [Figs. 2(e) and 2(f)].

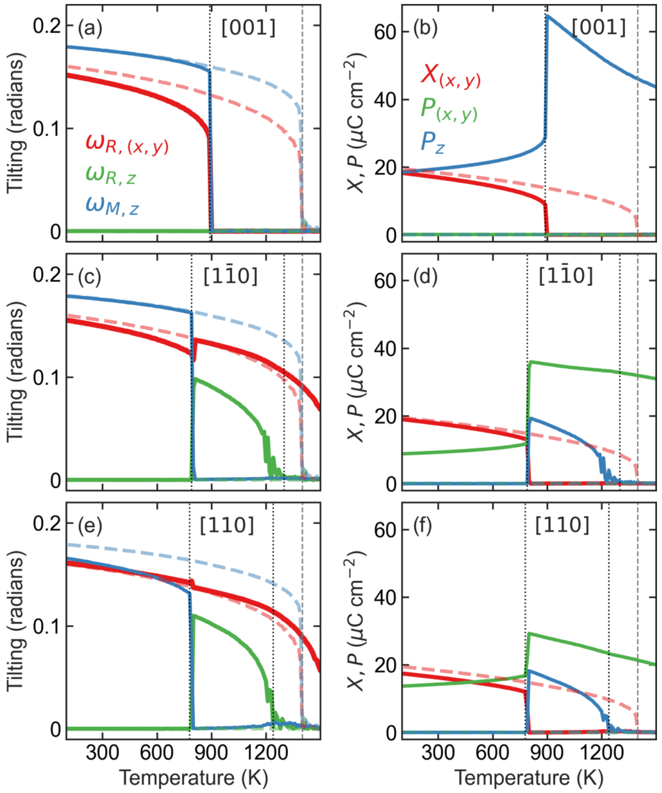

FIG. 2. Effect of $\mathcal{E}$ field on the temperature dependence of the order parameters. (a), (b) [001] field of 0.87 MV cm^{-1} (solid lines) in comparison with zero field (dashed lines). (c), (d) Same for [1$\bar{1}$0] field of 0.87 MV cm^{-1}. (e), (f) Same for [110] field of 0.61 MV cm^{-1}. The four relevant order parameters are antiphase octahedral tilting ω_R, in-phase tilting ω_M, polarization P, and antiferroelectric vector X. Note that $P_x = -P_y$ for [1$\bar{1}$0] field. The vertical dotted (or dashed) lines delimit different phases under finite (or zero) field.

B. Decomposed contributions to the electrocaloric effect

Let us now concentrate on the ECE coefficient $\alpha = \frac{\partial T}{\partial \mathcal{E}}|_S$ with T being temperature and S being entropy, which can be calculated from the cumulant formula using outputs of the MC simulations [30,36–38],

$$\alpha_{\mathrm{MC}} = -Z^* a_{\mathrm{latt}} T \left\{ \frac{\langle |\boldsymbol{u}| E_{\mathrm{tot}}\rangle - \langle |\boldsymbol{u}|\rangle \langle E_{\mathrm{tot}}\rangle}{\langle E_{\mathrm{tot}}^2\rangle - \langle E_{\mathrm{tot}}\rangle^2 + \frac{21(k_B T)^2}{2N}} \right\}, \qquad (2)$$

where Z^* is the Born effective charge associated with the local mode, a_{latt} represents the lattice constant of the five-atom pseudocubic perovskite cell, T is the simulation temperature, $|\boldsymbol{u}|$ is the supercell average of the magnitude of the local mode, E_{tot} is the total energy given by the effective Hamiltonian, k_{B} is the Boltzmann constant, N is the number of sites in the supercell, and $\langle\ \rangle$ denotes average over the MC sweeps at a given temperature.

For fields applied along the [001] direction [Fig. 3(a)], similar to the case in PZO-based AFE [6,7], α is negative in the AFE-based state, and its magnitude increases with temperature, which maximizes at the transition point where the AFE-based state disappears. Across the phase transition, α jumps to be positive in the FE state, then (slightly) increases with temperature, as such qualitative temperature dependence is known for FEs [30].

To have insightful analysis of the ECE, Figs. 3(b) and 3(c) also report two other quantities related to electrocaloric response, namely, the total isothermal change in entropy ΔS, and the adiabatic temperature change ΔT, as well as their individual contributions. Practically, to be able to compute the total entropy change, we consider the following Landau model

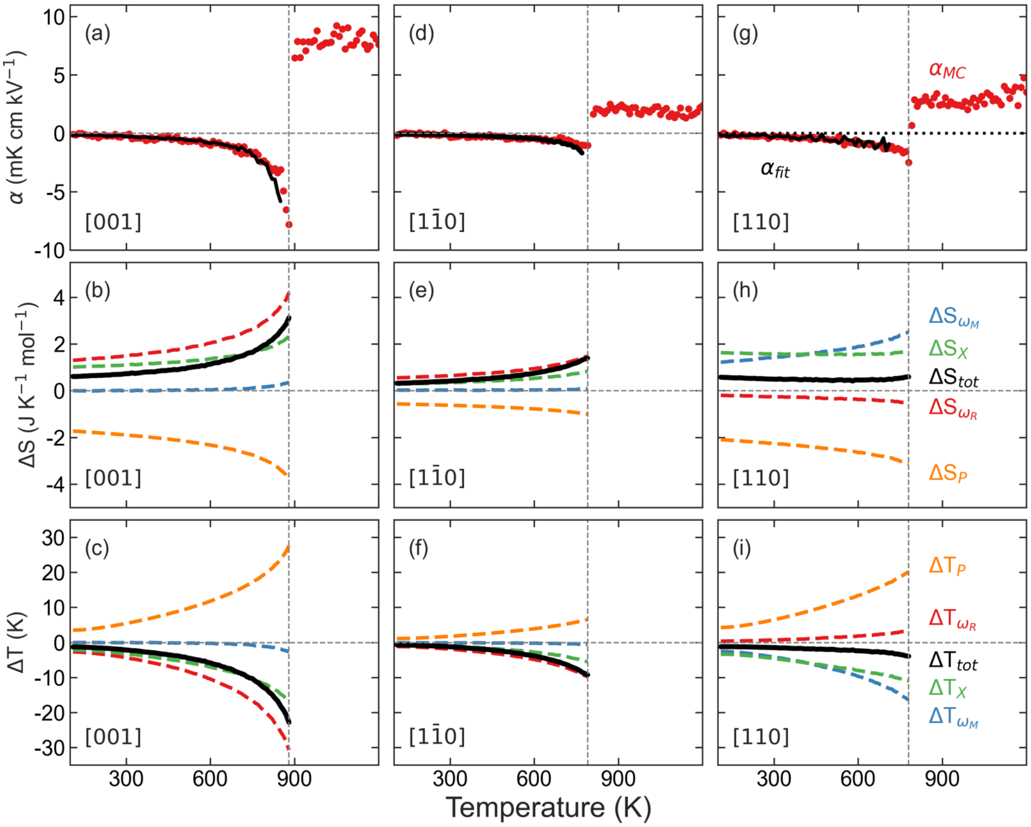

FIG. 3. Temperature dependence of the calculated ECE coefficient α, isothermal entropy change, and temperature change under various field directions. (a)–(c) [001] (0.87 MV cm^{-1}). (d)–(f) [1$\bar{1}$0] (0.87 MV cm^{-1}). (g)–(i) [110] (0.61 MV cm^{-1}) electric field. Colors in ΔS and ΔT denote the total and individual contributions from each order parameter. $\alpha_{\rm MC}$ is computed by the cumulant approach and $\alpha_{\rm fit}$ is a fitted curve based on the Landau model.

for *Pnma*-type AFE [35]:

$$\begin{aligned} F = {} & F_0 + \tfrac{1}{2}a_{\omega_R}(T)\omega_R^2 + \tfrac{1}{4}b_{\omega_R}\omega_R^4 + \tfrac{1}{2}a_{\omega_M}(T)\omega_M^2 + \tfrac{1}{4}b_{\omega_M}\omega_M^4 \\ & + \tfrac{1}{2}a_X(T)X^2 + \tfrac{1}{4}b_X X^4 + \tfrac{1}{2}a_P(T)P^2 + \tfrac{1}{4}b_P P^4 \\ & - \mathcal{E}P - cX\omega_R\omega_M + \tfrac{1}{2}d_1P^2\omega_R^2 + \tfrac{1}{2}d_2P^2\omega_M^2. \end{aligned} \tag{3}$$

Note that F_0 is the field-independent part of the free energy, only the quadratic coefficients $a_{\rm op} = A_{\rm op}(T - T_0^{\rm op})$ have explicit temperature dependence, with op being the order parameter of ω_R, ω_M, P, or X, respectively, and $T_0^{\rm op}$ is a transition temperature for each order parameter. Also note that the tiltings are known to be the primary order parameters in many *Pnma* systems, while X is secondary arising from the $cX\omega_R\omega_M$ trilinear coupling involving in-phase and antiphase tiltings [39]. Recalling that $S = -\frac{\partial F}{\partial T}|_{\mathcal{E},{\rm op}}$, the change of entropy associated with a change of $\mathcal{E}$ can be written as

$$\begin{aligned} \Delta S(T) = {} & -A_{\omega_R}\left[\omega_R^2(T,\mathcal{E}_2) - \omega_R^2(T,\mathcal{E}_1)\right] \\ & -A_{\omega_M}\left[\omega_M^2(T,\mathcal{E}_2) - \omega_M^2(T,\mathcal{E}_1)\right] \\ & -A_P[P^2(T,\mathcal{E}_2) - P^2(T,\mathcal{E}_1)] \\ & -A_X[X^2(T,\mathcal{E}_2) - X^2(T,\mathcal{E}_1)] \\ = {} & \Delta S_{\omega_R} + \Delta S_{\omega_M} + \Delta S_P + \Delta S_X, \end{aligned} \tag{4}$$

where $\mathcal{E}_1$ and $\mathcal{E}_2$ are the initial and final electric field, respectively, and the values of the order parameters are obtained from MC simulations. The adiabatic temperature change due to ECE can be further obtained via $\Delta T = -(T/C_{\mathcal{E}})\Delta S$, where $C_{\mathcal{E}}$ is the phonon-specific heat [40]—which is calculated here by density functional theory (see SM Sec. S3 [20]). We thus have

$$\Delta T = -\frac{T}{C_{\mathcal{E}}}\Delta S = \Delta T_{\omega_R} + \Delta T_{\omega_M} + \Delta T_P + \Delta T_X. \tag{5}$$

Equations (4) and (5) are used to evaluate the entropy and temperature change (as well as their individual contributions associated with ω_R, ω_M, P, and X), in which each order parameter is directly obtained from MC simulations while the coefficients $A_{\rm op} = -a_{\rm op}^{\text{0-K}}/T_0^{\rm op}$ are extracted by the following two steps: (1) finding $a_{\rm op}^{\text{0-K}}$ from fitting the 0 K double-well energies based on our effective Hamiltonian to the Landau model [Eq. (3)] and (2) determining $T_0^{\rm op}$ from fitting α calculated from the cumulant formula to that based on the Landau model with $\alpha_{\rm fit} = \Delta T/(2\Delta\mathcal{E})$ for $\Delta\mathcal{E}$=0.02 MV cm^{-1} (see SM Sec. S4 for details [20]). Note that $\alpha_{\rm fit}$ is shown in Fig. 3(a) and agrees rather well (over a large temperature range) with the α directly obtained from the MC simulations in the AFE-based state, therefore demonstrating the relevance of the aforementioned Landau model. Also note that the obtained $T_0^{\rm op}$ reflects the depth of the energy wells.

One can then realize from Eq. (5) two important features for each $\Delta T_{\rm op}$ associated with a specific order parameter (op): (1) such change is directly proportional to the $A_{\rm op}$ coefficient related to that order parameter and (2) such change involves the difference in the square of the order parameter between two electric fields, e.g., $[\omega_R^2(T,\mathcal{E}_2)-\omega_R^2(T,\mathcal{E}_1)]$ for the antiphase tilting. These four different individual changes in temperature are reported in Fig. 3(c) for fields along [001].

Here we only focus on the ECE in the AFE state, since latent heat needs to be considered when first-order AFE-to-FE transition occurs—which is not included in Eq. (4). Therefore, ECE involving the FE and PE states are not investigated within the scope of the present paper. ΔS and ΔT in Figs. 3(b) and 3(c), respectively, are practically calculated from Eqs. (4) and (5) with $\mathcal{E}_1$=0 and $\mathcal{E}_2$=0.87 MV cm^{-1} being along [001]. We numerically find that ΔT is negative and bears a qualitatively similar T dependence as that of α, i.e., its magnitude increases with increasing temperature and maximizes at the transition point. On the other hand, ΔS has an opposite sign to that of ΔT, as dictated by their relationship $\Delta T = -(T/C_{\mathcal{E}})\Delta S$. To understand how ECE is contributed by each order parameter, we can focus on the different ΔT_{op} displayed in Fig. 3(c). For this [001] field direction, ω_R, ω_M, and X show negative contributions, with the magnitude from ω_R being the largest and that from ω_M being negligible, together with the rather large positive contribution from P. According to Eq. (5), the negative (or positive) signs of the four different ΔT_{op} can be understood by the fact that the corresponding order parameter is suppressed (or enhanced) with the application of the field. In fact, as suggested by Eqs. (4) and (5), a large magnitude of ΔT_{op} relies on two factors, either those with large field-induced changes in their order parameter such as ω_R and P here, or those with large coefficient A_{op} such as X here (op with large coefficient A_{op} is expected to have strongly T-dependent change of the corresponding vibrational entropy), whereas ΔT_{ω_M} for field along [001] is negligible since both A_{ω_M} and the field-induced change in ω_M are very small.

The same procedure is adopted to study the field directions along [$1\bar{1}0$] and [110]. For the [$1\bar{1}0$] field, as shown in Figs. 3(d)–3(f), a qualitatively similar ECE behavior is found compared with those from the [001] field (namely, a negative α having a magnitude increasing when approaching the AFE-to-FE transition), except that the predicted α, ΔS, and ΔT are smaller in magnitude, e.g., the largest negative $\alpha = -1.0$ mK kV cm^{-1}, $\Delta T = -9.2$ K for the [$1\bar{1}0$] field, to be compared with -7.8 mK kV cm^{-1} and -22.8 K for the [001] field, respectively; however, the relative contributions of the order parameters share qualitatively similar characteristics, i.e., ω_R and X are associated to negative ΔT_{ω_R} and ΔT_X, respectively, with ω_R contributing the most, together with the opposite effect from P (positive ΔT_P) and negligible contribution from ω_M (i.e., weak ΔT_{ω_M}). Note that α and ΔT are also negative and increase in magnitude with T within the AFE-based state for the [110] field [Figs. 3(g)–3(i)], and their magnitude is about -2.5 mK kV cm^{-1} and -3.9 K, respectively, at the transition point.

However, albeit the qualitative similarities from the sign of ΔT_P and ΔT_X for all three $\mathcal{E}$ directions considered in Fig. 3, ΔT_{ω_R} becomes positive and ΔT_{ω_M} shows a large negative contribution only for $\mathcal{E}$ along [110]. Such unique features are associated to the small enhancement of ω_R and large suppression of ω_M under [110] fields [see Fig. 2(e)]. Further, the small ECE for [110] field can be well understood by the fact that the negative ΔT_{ω_M} and ΔT_X contributions are largely canceled by the positive ΔT_P and ΔT_{ω_R} contributions. It is also worth mentioning that ΔT_P is always positive and ΔT_X is always negative, as P increases while X decreases upon application of the $\mathcal{E}$ field [see Eq. (5)]. In other words, being consistent with Eq. (4), the applied field makes P more ordered and X more disordered.

C. Relative electrocaloric contributions due to the field direction

It is interesting to note that the contrast of different ECE behaviors from various field directions are related to the relative orientation between $\mathcal{E}$ and X; for instance, [001] and [$1\bar{1}0$] fields are perpendicular to the antipolar vector, whereas the [110] field is parallel to it. As detailed in SM Sec. S5 [20], via the calculated energy landscape, we show numerically that minimization of the total energy dictates that increasing P_z or $P_{(x,\bar{y})}$ in the *Pnma* state would strongly suppress ω_R, whereas such suppression is much less for ω_M; and in contrast, the opposite is found for $P_{(x,y)}$, i.e., ω_M is strongly suppressed but ω_R is less correlated when $P_{(x,y)}$ increases.

In fact, a continuous variation of ΔT_{op} can be realized if the $\mathcal{E}$ direction changes from [110] toward [001]. In Fig. 4, we include results for $\mathcal{E}$ lying along [111], [112], [113], and [114] directions (see SM Sec. S6 for further details [20]). While the overall ΔT remains negative and ΔT_P is always positive (because P always increases with the field in the AFE-based phase), ΔT_{ω_R} becomes more negative while ΔT_{ω_M} becomes less negative, as the angle between $\mathcal{E}$ and X changes from 0 to 90 degrees. Nonetheless, it is worth noting that the contributions associated to X and P also show opposite trends with such rotation of the field, i.e., ΔT_P decreases (less positive) and ΔT_X increases (less negative).

D. Electrocaloric temperatures under various electric fields

For each field direction, we can further change the field strength to tune the AFE transition temperature, where the maximum ECE occurs, thus manipulating the negative ECE. As depicted in Fig. 5, for $\mathcal{E}$ along [001], [$1\bar{1}0$], and [110], the maximized negative ΔT is given by intermediate field, which allows the AFE-to-FE transition to occur at a rather high temperature. More precisely, if $\mathcal{E}$ is too small, the FE state is absent; if $\mathcal{E}$ is too large, the AFE-to-FE transition happens at low temperature and ΔT is relatively small. Remarkably, ΔT is predicted to reach -29.0 K if $\mathcal{E}$ is along [001] with a magnitude of 0.70 MV cm^{-1} at 1100 K, therefore being very large compared with the previously reported value of -5.8 K in La-doped Pb(Zr,Ti)O$_3$ [6]. However, if one is interested in a large negative ECE at RT, a specific field direction and strength should be chosen, e.g., the largest negative ΔT of -4.7 K is realized at RT with a [001] field having a magnitude of 1.13 MV cm^{-1}, with which the AFE-to-FE transition is close to RT. This value is comparable to that of PZO-based AFEs at RT [6,7].

E. Discussion

Finally, let us examine the two previously proposed mechanisms. Regarding the dipole-canting mechanism [6], we

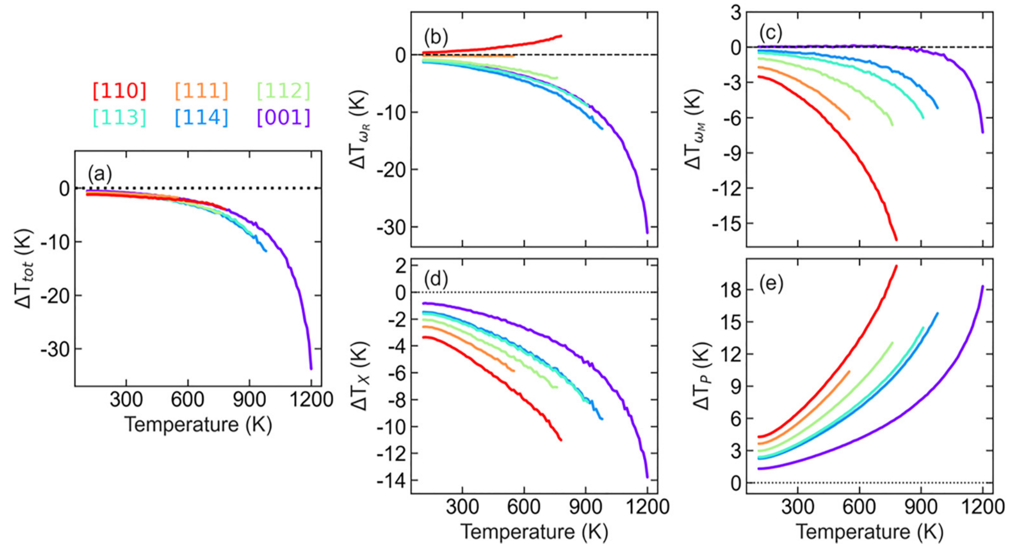

FIG. 4. Calculated ECE contributions from each order parameter for additional $\mathcal{E}$-field directions from [110] to [001]. The field directions include [110], [111], [112], [113], [114], and [001], with a magnitude of 0.61 MV cm^{-1}. (a) ΔT_{tot}. (b) ΔT_{ω_R}. (c) ΔT_{ω_M}. (d) ΔT_X. (e) ΔT_P.

compute the statistical distribution of dipole orientations under zero and applied fields at 300 K (see Methods section and Fig. 6). Under zero field [Figs. 6(a) and 6(b)], the system is AFE with dipoles in opposite directions, denoted as right and left dipoles [layers with blue and yellow arrows in Fig. 1(a)], being close to the [110] and [$\bar{1}\bar{1}$0] directions, respectively. Due to temperature effect, the maximum probability for either right or left dipoles corresponds to a small but finite angle (12 degrees). For illustration purposes, we label angles above the (001) plane as positive and below the (001) plane as negative and, as expected, the distribution is symmetric about zero angle, indicating that the most probable dipole orientations form a cone around the [110] direction. When a [110] field of 0.61 MV cm^{-1} being parallel to the antipolar vector is applied, as shown in Figs. 6(c) and 6(d), the distribution of right dipoles obviously narrows (peaks at 9 degrees) while significantly broadening for the left dipoles, since they are, respectively, in the same and opposite directions to the applied field. This picture is fully in line with the dipole canting model in Ref. [6]. However, we numerically find that if only the dipole degrees of freedom (i.e., right and left dipoles or, equivalently, P and X) are considered, ΔT_P and ΔT_X have opposite signs [Fig. 3(i)], but the response of P to $\mathcal{E}$ field is much greater than X. The corresponding change of temperature ($\Delta T_P + \Delta T_X$) is thus always positive, instead of negative, which therefore cannot explain the overall negative ECE.

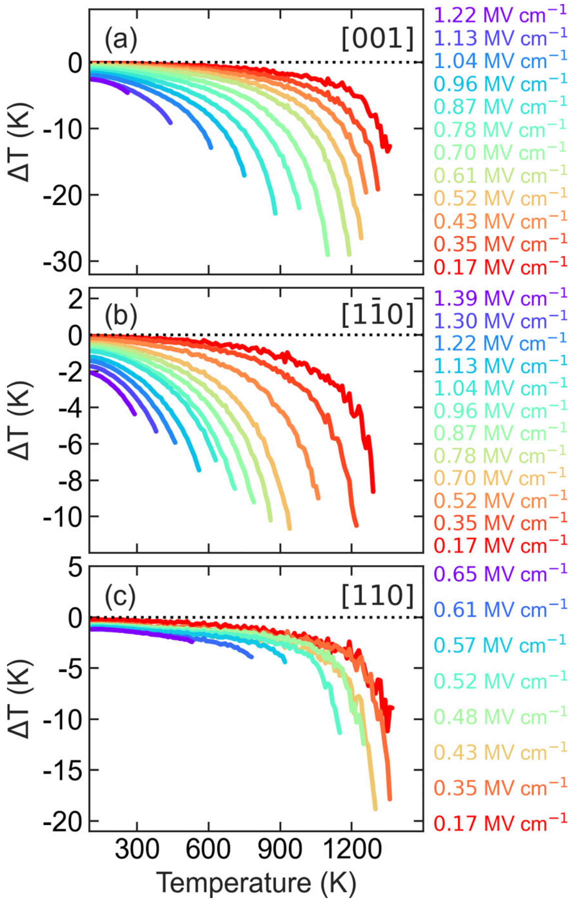

FIG. 5. The ECE temperature change as a function of temperature under various electric field magnitude and directions. (a) [001], (b) [1$\bar{1}$0], and (c) [110] field.

If the field with a strength of 0.87 MV cm^{-1} is along [001] or [1$\bar{1}$0], i.e., being perpendicular to the antipolar vector, the distribution becomes singly peaked with a Gaussian shape and shifts expectedly toward the field direction [Figs. 6(e)–6(h)]. The spreads are similar for both field directions, as well as for the right and left dipoles, which are slightly narrower than the overall spread at zero field. For these two perpendicular $\mathcal{E}$ directions, ΔT_P and ΔT_X also show opposite signs [Figs. 3(c) and 3(f)], and the change of temperature ($\Delta T_P + \Delta T_X$) is again positive rather than negative. This observation strongly suggests that explicit consideration of octahedral degrees of freedom is mandatory to correctly account for the (negative) ECE in AFEs. The statistical distributions of the octahedral tiltings are also calculated [Figs. 6(i) and 6(j)], which are typical Gaussian functions and show little change in the width with application of the field, except the small shifts of the

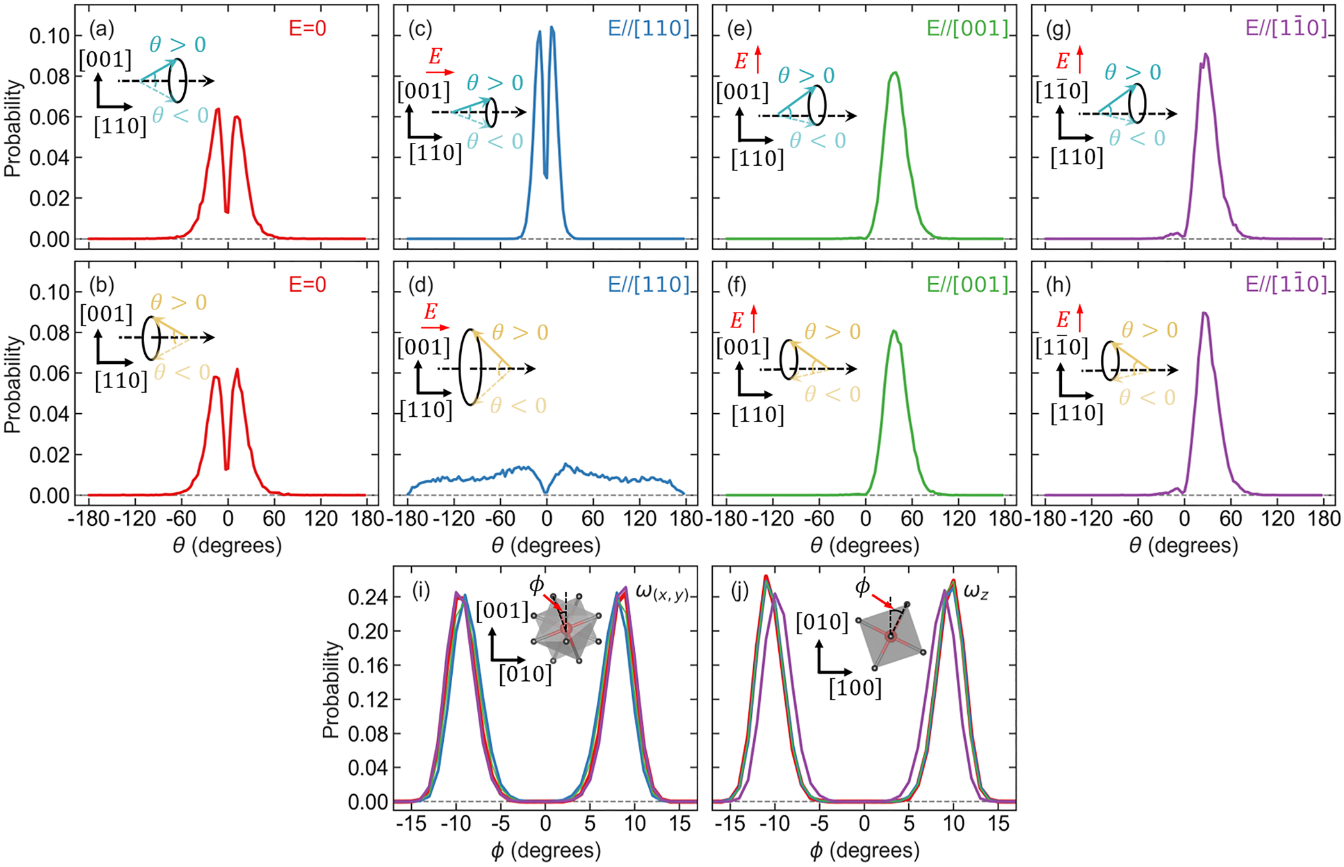

FIG. 6. Statistical distribution of electric dipolar orientations and octahedral tilting angles under zero and finite electric fields at 300 K. (a) Angles between the right (blue) dipoles and [110] direction under zero field. (b) Angles between the left (yellow) dipoles and [$\bar{1}\bar{1}0$] direction under zero field. (c), (d) Same under [110] field of 0.61 MV cm^{-1}. (e), (f) Same under [001] field of 0.87 MV cm^{-1}. (g), (h) Same under [1$\bar{1}$0] field of 0.87 MV cm^{-1}. The insets illustrate the meaning and relative changes of the positive and negative angles. The field directions are drawn as red arrows. (i) Distribution of the in-plane octahedral tilting angles under zero and finite fields of various directions. (j) Distribution of the out-of-plane octahedral tilting angles under zero and finite fields of various directions. Same color schemes are used for dipoles and octahedral tilting angles.

maxima that are consistent with the average values reported in Figs. 2(a), 2(c), and 2(e).

On the other hand, the perturbative approach solely based on polarization (as functions of $\mathcal{E}$ field and temperature) [11] agrees reasonably well with our predictions at low fields (see SM Sec. S7 [20]), justifying the numerical accuracy of the present method and indicating that the Maxwell relation $\frac{\partial S}{\partial \mathcal{E}}|_T = \frac{\partial P}{\partial T}|_{\mathcal{E}}$ holds for negative ECE systems with contributions from multiple degrees of freedom.

IV. CONCLUSIONS

In summary, our quantitative method shows that, as octahedral tiltings are often primary order parameters in AFE perovskites, they have to be taken explicitly into account to construe the negative ECE, and mere inclusion of dipolar degrees of freedom is insufficient. We also predict that AFE BNFO solid solutions are very promising to achieve a giant temperature decrease near the AFE transition upon application of an electric field. Our atomistic mechanism also suggests that all *Pnma*-type perovskites (e.g., $CaTiO_3$), irrespective of whether or not they are AFE, should yield negative ECE, and enhanced negative ECE may be possible upon freezing or suppression of order parameter(s) with positive ΔT_{op}, for instance, via interfacial proximity effect.

ACKNOWLEDGMENTS

This work is supported by the National Natural Science Foundation of China under Grant No. 12074277, Natural Science Foundation of Jiangsu Province (No. BK20201404), the startup fund from Soochow University and the support from Priority Academic Program Development (PAPD) of Jiangsu Higher Education Institutions. L.B. thanks the Office of Naval Research for support under Grant No. N00014-21-1-2086 and the Vannevar Bush Faculty Fellowship (VBFF) Grant No. N00014-20-1-2834 from the Department of Defense. J.I. thanks the Luxembourg National Research Grant for support under Grant No. FNR/C18/MS/12705883/REFOX.

[1] J. Shi, D. Han, Z. Li, L. Yang, S.-G. Lu, Z. Zhong, J. Chen, Q. Zhang, and X. Qian, Joule **3**, 1200 (2019).

[2] T. Correlia and Q. Zhang, *Electrocaloric Materials: New Generation of Coolers* (Springer, Berlin, 2014).

[3] S. Fähler, U. K. Rößler, O. Kastner, J. Eckert, G. Eggeler, H. Emmerich, P. Entel, S. Müller, E. Quandt, and K. Albe, Adv. Eng. Mater. **14**, 10 (2012).

[4] X. Moya, S. Kar-Narayan, and N. D. Mathur, Nat. Mater. **13**, 439 (2014).

[5] R. Pirc, B. Rožič, J. Koruza, B. Malič, and Z. Kutnjak, Europhys. Lett. **107**, 17002 (2014).

[6] W. Geng, Y. Liu, X. Meng, L. Bellaiche, J. F. Scott, B. Dkhil, and A. Jiang, Adv. Mater. **27**, 3165 (2015).

[7] P. Vales-Castro, R. Faye, M. Vellvehi, Y. Nouchokgwe, X. Perpiñà, J. M. Caicedo, X. Jordà, K. Roleder, D. Kajewski, A. Perez-Tomas *et al.*, Phys. Rev. B **103**, 054112 (2021).

[8] T. Gottschall, A. Gracia-Condal, M. Fries, A. Taubel, L. Pfeuffer, L. Manosa, A. Planes, K. P. Skokov, and O. Gutfleisch, Nat. Mater. **17**, 929 (2018).

[9] M. Marathe, D. Renggli, M. Sanlialp, M. O. Karabasov, V. V. Shvartsman, D. C. Lupascu, A. Grünebohm, and C. Ederer, Phys. Rev. B **96**, 014102 (2017).

[10] A. Grünebohm, Y.-B. Ma, M. Marathe, B.-X. Xu, K. Albe, C. Kalcher, K.-C. Meyer, V. V. Shvartsman, D. C. Lupascu, and C. Ederer, Energy Technol. **6**, 1491 (2018).

[11] M. Graf and J. Íñiguez, Commun. Mater **2**, 60 (2021).

[12] C. Milesi-Brault, C. Toulouse, E. Constable, H. Aramberri, V. Simonet, S. de Brion, H. Berger, L. Paolasini, A. Bosak, J. Iñiguez, and M. Guennou, Phys. Rev. Lett. **124**, 097603 (2020).

[13] B. Xu, O. Hellman, and L. Bellaiche, Phys. Rev. B **100**, 020102(R) (2019).

[14] M. W. Lufaso and P. M. Woodward, Acta Crystallogr., Sect. B: Struct. Sci **57**, 725 (2001).

[15] L. Bellaiche and J. Íñiguez, Phys. Rev. B **88**, 014104 (2013).

[16] A. Planes, T. Castan, and A. Saxena, Philos. Mag. **94**, 1893 (2014).

[17] J. Zhang, A. Heitmann, S. Alpay, and G. Rossetti Jr, Integr. Ferroelectr. **125**, 168 (2011).

[18] Y.-B. Ma, N. Novak, J. Koruza, T. Yang, K. Albe, and B.-X. Xu, Phys. Rev. B **94**, 100104(R) (2016).

[19] A. Edström and C. Ederer, Phys. Rev. Lett. **124**, 167201 (2020).

[20] See Supplemental Material at http://link.aps.org/supplemental/10.1103/PhysRevB.106.224107 for (1) computational details, (2) temperature dependencies of the order parameters for various fields, (3) DFT-calculated specific heat, (4) determination of parameters in the Landau free-energy model, (5) correlation between polarization and octahedral tiltings, (6) additional $\mathcal{E}$-field directions from [110] to [001] pseudo-cubic directions, and (7) comparison with a previously proposed perturbative approach, which additionally includes Refs. [11,21–30,34,36–38,41–54].

[21] S. Prosandeev, D. Wang, W. Ren, J. Íñiguez, and L. Bellaiche, Adv. Funct. Mater. **23**, 234 (2013).

[22] D. Albrecht, S. Lisenkov, W. Ren, D. Rahmedov, I. A. Kornev, and L. Bellaiche, Phys. Rev. B **81**, 140401(R) (2010).

[23] I. A. Kornev, S. Lisenkov, R. Haumont, B. Dkhil, and L. Bellaiche, Phys. Rev. Lett. **99**, 227602 (2007).

[24] S. Lisenkov, D. Rahmedov, and L. Bellaiche, Phys. Rev. Lett. **103**, 047204 (2009).

[25] W. Zhong, D. Vanderbilt, and K. M. Rabe, Phys. Rev. Lett. **73**, 1861 (1994).

[26] W. Zhong and D. Vanderbilt, Phys. Rev. Lett. **74**, 2587 (1995).

[27] I. A. Kornev, L. Bellaiche, P.-E. Janolin, B. Dkhil, and E. Suard, Phys. Rev. Lett. **97**, 157601 (2006).

[28] B. Xu, D. Wang, J. Íñiguez, and L. Bellaiche, Adv. Funct. Mater. **25**, 552 (2015).

[29] D. Kan, V. Anbusathaiah, and I. Takeuchi, Adv. Mater. **23**, 1765 (2011).

[30] Z. Jiang, B. Xu, S. Prosandeev, Y. Nahas, S. Prokhorenko, J. Íñiguez, and L. Bellaiche, Phys. Rev. B **103**, L100102 (2021).

[31] S. Karimi, I. Reaney, Y. Han, J. Pokorny, and I. Sterianou, J. Mater. Sci. **44**, 5102 (2009).

[32] S. Karimi, I. Reaney, I. Levin, and I. Sterianou, Appl. Phys. Lett. **94**, 112903 (2009).

[33] D. Kan, L. Pálová, V. Anbusathaiah, C. J. Cheng, S. Fujino, V. Nagarajan, K. M. Rabe, and I. Takeuchi, Adv. Funct. Mater. **20**, 1108 (2010).

[34] B. Xu, J. Íñiguez, and L. Bellaiche, Nat. Commun. **8**, 15682 (2017).

[35] B. Xu, D. Wang, H. J. Zhao, J. Íñiguez, X. M. Chen, and L. Bellaiche, Adv. Funct. Mater. **25**, 3626 (2015).

[36] Z. Jiang, S. Prokhorenko, S. Prosandeev, Y. Nahas, D. Wang, J. Íñiguez, E. Defay, and L. Bellaiche, Phys. Rev. B **96**, 014114 (2017).

[37] Z. Jiang, Y. Nahas, S. Prokhorenko, S. Prosandeev, D. Wang, J. Íñiguez, and L. Bellaiche, Phys. Rev. B **97**, 104110 (2018).

[38] S. Bin-Omran, I. A. Kornev, and L. Bellaiche, Phys. Rev. B **93**, 014104 (2016).

[39] H. J. Zhao, J. Íñiguez, W. Ren, X. M. Chen, and L. Bellaiche, Phys. Rev. B **89**, 174101 (2014).

[40] Z. Kutnjak, B. Rožič, and R. Pirc, in *Wiley Encyclopedia of Electrical and Electronics Engineering*, edited by J. G. Webster (Wiley, 2015).

[41] W. Zhong, D. Vanderbilt, and K. M. Rabe, Phys. Rev. B **52**, 6301 (1995).

[42] D. Rahmedov, D. Wang, J. Íñiguez, and L. Bellaiche, Phys. Rev. Lett. **109**, 037207 (2012).

[43] C. Daumont, W. Ren, I. Infante, S. Lisenkov, J. Allibe, C. Carrétéro, S. Fusil, E. Jacquet, T. Bouvet, F. Bouamrane *et al.*, J. Phys.: Condens. Matter **24**, 162202 (2012).

[44] G. Kresse and J. Furthmüller, Phys. Rev. B **54**, 11169 (1996).

[45] G. Kresse and J. Furthmüller, Comput. Mater. Sci. **6**, 15 (1996).

[46] P. E. Blöchl, Phys. Rev. B **50**, 17953 (1994).

[47] J. P. Perdew, K. Burke, and M. Ernzerhof, Phys. Rev. Lett. **77**, 3865 (1996).

[48] S. Baroni, P. Giannozzi, and A. Testa, Phys. Rev. Lett. **58**, 1861 (1987).

[49] S. Baroni, S. De Gironcoli, A. Dal Corso, and P. Giannozzi, Rev. Mod. Phys. **73**, 515 (2001).

[50] X. Gonze and J.-P. Vigneron, Phys. Rev. B **39**, 13120 (1989).

[51] X. Gonze and C. Lee, Phys. Rev. B **55**, 10355 (1997).

[52] A. Togo and I. Tanaka, Scr. Mater. **108**, 1 (2015).

[53] J. Íñiguez, M. Stengel, S. Prosandeev, and L. Bellaiche, Phys. Rev. B **90**, 220103(R) (2014).

[54] J. C. Wojde and J. Íñiguez, Phys. Rev. B **90**, 014105 (2014).